Magnetic resonance-based imaging of human electric properties with phaseless contrast source inversion

Magnetic resonance-based imaging of human electric properties with phaseless contrast source inversion.

To cite this article before publication: ALESSANDRO ARDUINO *et al* 2018 *Inverse Problems* in press https://doi.org/10.1088/1361-6420/aac536

Magnetic resonance-based imaging of human electric properties with phaseless contrast source inversion.

Alessandro Arduino[1,2], Oriano Bottauscio[2], Mario Chiampi[2] and Luca Zilberti[2]

[1] Dipartimento Energia, Politecnico di Torino, 10129 Torino, Italy
[2] Metrologia per la Qualità della Vita, Istituto Nazionale di Ricerca Metrologica, 10135 Torino, Italy

E-mail: alessandro.arduino@polito.it

17 April 2018

Abstract. Magnetic resonance imaging scanners can provide, by B1-mapping techniques, measurements of the transmit sensitivity magnitude, whereas the transmit sensitivity phase can only be approximated under symmetry assumptions of the coil and the sample. Nonetheless, up to now many techniques have been proposed to retrieve electric properties maps at radiofrequency by elaborating the complex transmit sensitivity. These techniques are usually referred to as magnetic resonance-based electric properties tomography. In order to perform imaging of the elecric properties also in cases which do not fulfill the assumptions for transmit sensitivity phase estimation, a variation of the phaseless contrast source inversion technique is proposed in this paper to retrieve the electric properties by elaborating only the magnitude of the transmit sensitivity. The novel technique is described in a generalised framework based on a functional viewpoint and it is specialised to deal with two-dimensional boundary-free problems. Moreover, a phaseless back propagation solution is proposed as initial guess. The proposed technique and initial guess have been tested on realistic two-dimensional model problems, which show that the numerical minimisation converges towards the global minimum when multiple linearly independent measurements are provided and that it is quite robust with respect to noisy inputs.

AMS classification scheme numbers: 78A46, 92C55, 35Q61

Keywords: Electric properties tomography, magnetic resonance imaging, phaseless contrast source inversion, global Maxwell tomography, phaseless back propagation

Submitted to: *Inverse Problems*

1. Introduction

In the last years, the scientific community has made many efforts to develop methods capable of measuring the distribution of the electric properties (EPs) inside a human

body at radiofrequency (RF). The increasing interest shown in this field is explained by the several applications that would benefit from the knowledge of the human EPs. From a clinical point of view, the RF electric conductivity has been proven to be an imaging biomarker [1] for invasive breast cancers [2] and malignant colorectal tissues [3]. Precisely, in both cases a significant increase in the electric conductivity with respect to the physiological state is experienced. Moreover, from a dosimetric point of view, most of the diagnostic and therapeutic medical devices and therapies that use RF electromagnetic fields, like oncological hyperthermia [4] or magnetic resonance imaging (MRI) [5], could take advantage from patient-specific maps of the EPs, both in treatment planning [6] and in safety monitoring [7].

The traditional approach to RF EPs imaging is the so-called microwave tomography. It consists in the solution of an inverse electromagnetic scattering problem [8], in which a set of transmit coils illuminates the investigated body and the resulting scattered field is measured by receiving antennas arranged around the body itself. Because microwave tomography is an ill-posed problem in the sense of Hadamard—precisely, there is no continuity of the EPs with respect to the scattered field [9]—, the obtainable images are affected by a maximum achievable resolution close to half the wavelength of the radiation in the imaged tissues [10]. Despite this limitation, microwave tomography is widely used in geology [11], non-destructive evaluation [12], through-wall imaging [13] and so on, but it has not been extensively used in the biomedical applications, where the desired resolution may be far from the maximum achievable.

The possibility to employ MRI measurements for the estimation of human EPs had been proposed for the first time in 1991 [14] and it has been rediscovered just in recent years [15]. In this way, the scattered field is measured inside the inspected body in a large amount of points leading to a potential increase in the achievable resolution [9]. In addition, the availability of so many measurement points likely removes during the solution of the inverse problem some local minima from the cost functional [16] usually minimised by local numerical methods, like steepest descent, quasi-Newton or conjugate-gradient methods. The EPs imaging starting from MRI measurements is typically referred to as magnetic resonance-based electric properties tomography (MREPT) and a plethora of strategies have been proposed for its practical implementation [10,15,17–21]. Because of the large amount of available measurements, the first solutions proposed are based on a direct elaboration of the measured data [15,17,18,21]. However, most of the recently proposed approaches are based on minimisation of cost functionals [10, 19, 20].

The main difference between MREPT and microwave tomography, besides the location of measurement points, is the nature of the measured data. Precisely, MRI scanners can measure the component of the RF magnetic field $\vec{B}_1$ that rotates in the same wise as the nuclear Larmor precession [5] only. This quantity is called transmit sensitivity of the RF coil and is denoted by B_1^+. By using a right-handed Cartesian coordinate system $(\hat{x}, \hat{y}, \hat{z})$ such that the negative $\hat{z}$-axis is directed as the static field of

the MRI scanner $\vec{B}_0$ [5], the transmit sensitivity can be described as [22]

$$B_1^+ = \frac{B_{1,x} + \mathrm{i}B_{1,y}}{2}\,, \tag{1}$$

where i is the imaginary unit and $B_{1,x}$ and $B_{1,y}$ are phasors. Actually, the magnitude of the transmit sensitivity can be measured without hypotheses, neither on the transmit coil, nor on the examined body, using a B1-mapping technique [23,24]. On the contrary, the few methods that have been proposed to measure the phase of B_1^+ are based on strong symmetry assumptions on the coil and the body [25–28]. As a consequence, the MREPT methods that assume the knowledge of the whole transmit sensitivity—both magnitude and phase—can be applied only to special contexts.

In order to overcome the transmit sensitivity phase issue, the local Maxwell tomography (LMT) has been proposed by including the phase recovery in the MREPT procedure by means of a direct and local elaboration of the measurable data [29, 30]. With the same interest in dealing with the lack of information about B_1^+, the global Maxwell tomography (GMT) has been proposed more recently as a cost minimisation framework, in which only the discrepancy with respect to the transmit sensitivity magnitude is considered [31]. The LMT and GMT methods have the merit of showing that the impossibility to perform phase measurements can be addressed by including it in the problem formulation, instead of looking for assumptions that bind the methods to particular cases. In this paper, the philosophy of GMT is implemented with a phaseless contrast source inversion (CSI) technique [32, 33].

The CSI technique has already been adapted to MREPT resulting in the method indicated as CSI-EPT [20], which has proven to be very accurate in EPs recovery [34] and robust in the treatment of noisy input [20, 35]. In addition to the EPs, CSI-EPT maps also the distribution of an auxiliary unknown—named contrast source—from which it is possible to deduce both the electric and the magnetic fields generated by the employed transmit coil. Thus, besides being an accurate imaging technique, CSI-EPT may also be a useful tool in MRI safety, because only simple algebraic manipulations of its output are needed for a patient-specific local specific absorption rate (SAR) evaluation [34, 36]. In fact, the peak value of local SAR in MRI scanners, which is limited by legal regulations like the international relevant standard IEC 60601-2-33 [37], should be monitored for safety assessment. Nowadays, it is estimated indirectly and not in a proper patient-specific sense [38], so that the adoption of CSI-EPT could lead to more accurate safety checks.

Despite its good features, the application of CSI-EPT in actual scanners is strongly affected by the need of measurements of the whole transmit sensitivity B_1^+, both magnitude and phase. Actually, to the best of the Authors' knowledge, the technique has never been tested *in vivo* up to now. With a view to reducing the input requirements of CSI-EPT while maintaining its desirable features, in this paper a variation of CSI-EPT that requires only the transmit sensitivity magnitude is proposed and, because of the strong relation with GMT, is denoted by the symbol CSI-GMT.

The paper is organised as follows. In section 2, the notation adopted throughout

the paper is described and a rigorous formulation of the CSI-GMT problem is provided in a functional point of view. Section 3 presents the numerical procedure employed to minimise the cost functional of the CSI-GMT problem in which as much terms as possible are computed analytically in order to reduce the computational burden. In addition, the phaseless back propagation is proposed as a new informative initial guess and it is compared with other initial guesses previosly presented in literature. The method is extended to handle multiple inputs in section 4. In section 5, CSI-GMT is applied to two-dimensional model problems in which a slice of a human body is radiated by unshielded transmit coils. The operators introduced in the previous sections are specialised for these particular cases. The results show that the adoption of multiple measurements solves the issue of local minima in the cost functional and improves the robustness of the method against noisy inputs. Finally, in section 6, the content of the paper is summarised and the next steps in this research field are outlined.

2. Problem formulation

Despite the CSI technique is usually described for homogeneous boundary-free backgrounds, it has greater generality and just relies on the linearity of the partial differential equations (PDEs) of the direct problem. This fact can be easily understood looking at the CSI implementations based on alternative numerical methods instead of the classic convolutions of dyadic Green's functions [13, 39]. In order to place greater emphasis to this generality, the CSI-GMT problem is proposed with reference to a functional point of view, which makes no assumptions on the physical problem other than the needed ones. The same way forward has been followed in describing a general framework for CSI-EPT [40].

2.1. Direct problem

The RF fields measured by MRI scanners are described by Maxwell's equations, which constitute the direct problem at the basis of CSI-GMT as it is shown in this section.

The RF transmit coil of an MRI scanner is assumed to be immersed in a linear, isotropic and possibly heterogeneous background, extending in a domain Ω. Known values of permittivity $\varepsilon_{\mathrm{b}}(\vec{p})$ and conductivity $\sigma_{\mathrm{b}}(\vec{p})$ are assigned to each position $\vec{p} \in \Omega$ in the background, which is assumed to be magnetically neutral with constant vacuum permeability μ_0. Since the transmit coil operates at the Larmor frequency—which changes with the intensity of the static field $\vec{B}_0$, but is fixed for a given scanner—, it is convenient to exploit the time-harmonic domain assuming an omitted time factor $\exp(\mathrm{i}\omega t)$, where ω denotes the angular frequency of the electromagnetic radiation. Thus, the EPs can be assembled in the complex permittivity $\tilde{\varepsilon}_{\mathrm{b}}(\vec{p}) = \varepsilon_{\mathrm{b}}(\vec{p}) - \mathrm{i}\sigma_{\mathrm{b}}(\vec{p})/\omega$. The electromagnetic field generated by the coil in the background is the solution of the linear Maxwell's equations with proper forcing terms and linear boundary conditions on $\partial\Omega$, or at infinity for unbounded domains. This field is named the incident field and is denoted

by $\{\vec{E}^{\mathrm{i}}(\vec{p}), \vec{B}^{\mathrm{i}}(\vec{p})\}$.

The examined body is still assumed to be non-magnetic (*i.e.*, $\mu(\vec{p}) \equiv \mu_0$), as it is reasonable for biological tissues [41], with linear and isotropic electric properties. Thus, the presence of the body replaces the background electric properties in each position $\vec{p} \in \Omega$ with the unknown complex permittivity $\tilde{\varepsilon}(\vec{p}) = \varepsilon(\vec{p}) - \mathrm{i}\sigma(\vec{p})/\omega$ of the tissues. The body, when inserted in the domain, alters the electromagnetic field generated by the transmit coil even if it operates under the same conditions of the incident field, namely with the same boundary conditions and forcing terms. This altered field is called total field and is indicated as $\{\vec{E}(\vec{p}), \vec{B}(\vec{p})\}$. Unless the dependence on position of the defined maps is not trivial, it is omitted from now on.

The distortion of the total field with respect to the incident field due to the presence of the body is named scattered field and is defined as $\{\vec{E}^{\mathrm{s}}, \vec{B}^{\mathrm{s}}\} = \{\vec{E} - \vec{E}^{\mathrm{i}}, \vec{B} - \vec{B}^{\mathrm{i}}\}$. Thanks to the linearity of Maxwell's equations for the incident and the total fields, an equivalent problem for the scattered field is obtained by subtracting the total and the incident problems,

$$\begin{cases} \mathrm{rot}\ \vec{\mathrm{E}}^{\mathrm{s}} = -\mathrm{i}\omega\mu_0\vec{\mathrm{H}}^{\mathrm{s}} \\ \mathrm{rot}\ \vec{\mathrm{H}}^{\mathrm{s}} = \mathrm{i}\omega\tilde{\varepsilon}_{\mathrm{b}}\vec{\mathrm{E}}^{\mathrm{s}} + \vec{\mathrm{J}}^{\mathrm{s}} \end{cases} \tag{2}$$

where $\vec{H}^{\mathrm{s}} = \vec{B}^{\mathrm{s}}/\mu_0$ is the scattered magnetic field strength and $\vec{J}^{\mathrm{s}} = \mathrm{i}\omega\tilde{\varepsilon}_{\mathrm{b}}\vec{w}$ is an equivalent scattering current density, defined by means of the contrast source $\vec{w} = \chi\vec{E}$ and the contrast of the body $\chi = \tilde{\varepsilon}_{\mathrm{b}}^{-1}(\tilde{\varepsilon} - \tilde{\varepsilon}_{\mathrm{b}})$. The system of equations (2) is accompanied by the homogeneous version of the same boundary conditions of the incident and the total field problems, because the forcing terms, equal in the two cases, cancel each other out in the scattered field problem.

Under the assumption that the contrast source $\vec{w}$ is known and that reasonable boundary conditions are used, the PDEs problem for the scattered field has one and only one solution, which depends continuously on $\vec{w}$ [42, 43]. Using elements of functional analysis [44], this fact is equivalent to state that there exists a couple of linear and bounded operators $\mathcal{S}_{\mathrm{e}}$ and $\mathcal{S}_{\mathrm{h}}$ such that

$$\vec{E}^{\mathrm{s}} = \mathcal{S}_{\mathrm{e}}\vec{w}\,, \qquad \vec{H}^{\mathrm{s}} = \mathcal{S}_{\mathrm{h}}\vec{w}\,. \tag{3}$$

2.2. Inverse problem

The CSI-GMT inverse problem consists in recovering the distributions of the contrast source $\vec{w}$ and the contrast χ starting from the knowledge of the whole incident field $\{\vec{E}^{\mathrm{i}}, \vec{B}^{\mathrm{i}}\}$ and the magnitude of the transmit sensitivity $|B_1^+|$. The incident field can be measured or, more likely, simulated just once and used as a characterisation of the RF transmit coil. The transmit sensitivity magnitude, instead, is measured in presence of the examined body by a B1-mapping technique [23, 24]. The inversion is performed casting the problem in a minimisation one, based on the direct problem summarised by relations (3).

In order to quantify the discrepancy between the scattered field due to a guess contrast source $\vec{w}\,'$ and the measured transmit sensitivity, it is convenient to introduce a couple of linear operators. Inspired by (1), the operator $\mathcal{P}$ maps any vector field $\vec{u}$ into its positively rotating component,

$$\mathcal{P}\vec{u} = \frac{u_x + \mathrm{i}u_y}{2}\,. \tag{4}$$

Moreover, since the B1-mapping techniques measure the transmit sensitivity in a finite number N of points $(\vec{p}_i)_{i=1}^N$ that fall inside the examined body and are arranged on a Cartesian grid, an observation operator $\mathcal{O}$ that evaluates its input u in the measurement points is introduced [40],

$$\mathcal{O}u = (u(\vec{p}_i))_{i=1}^N\,. \tag{5}$$

Thus, the so-called data residual for the guess contrast source $\vec{w}\,'$ is defined as

$$\rho[\vec{w}\,'] = |H^+|^2 - |\mathcal{O}\mathcal{S}_\mathrm{h}^+\vec{w}\,' + H^{+;\mathrm{i}}|^2\,, \tag{6}$$

where $|H^+|^2 = |B_1^+|^2/\mu_0^2$, the observed positively rotating component of the incident field $H^{+;\mathrm{i}} = \mathcal{O}\mathcal{P}\vec{H}^\mathrm{i}$ and the composed operator $\mathcal{S}_\mathrm{h}^+ = \mathcal{P}\mathcal{S}_\mathrm{h}$ are used. It is worth noting that both magnitude and phase of $H^{+;\mathrm{i}}$ are used in data residual definition. This can be done because the whole incident field is provided by characterisation of the RF transmit coil. As can be seen from the next section, the square of the magnitude is employed in order to guarantee the analitical computation of the gradients of the cost functional [33, 45]. Clearly, the data residual is null for the actual contrast source $\vec{w}$.

On the other hand, the state residual, which takes into account a guess contrast $\chi\,'$ associated to a guess contrast source $\vec{w}\,'$, is easily derived noting that by definition

$$\vec{w} = \chi\vec{E} = \chi\vec{E}^\mathrm{i} + \chi\vec{E}^\mathrm{s} = \chi\vec{E}^\mathrm{i} + \chi\mathcal{S}_\mathrm{e}\vec{w}\,. \tag{7}$$

Thus, the state residual is

$$\vec{r}[\vec{w}\,', \chi\,'] = \chi\,'\vec{E}^\mathrm{i} + \chi\,'\mathcal{S}_\mathrm{e}\vec{w}\,' - \vec{w}\,', \tag{8}$$

and it is nullified by the actual contrast source $\vec{w}$ and contrast χ.

By combining the two residuals, the cost functional whose minimum solves the CSI-GMT problem is defined as follows,

$$F[\vec{w}\,', \chi\,'] = \underbrace{\frac{\eta_\mathrm{d}}{2}\|\rho[\vec{w}\,']\|_\mathbb{D}^2}_{F_\mathrm{d}[\vec{w}\,']} + \underbrace{\frac{\eta_\mathrm{s}[\chi\,']}{2}\|\vec{r}[\vec{w}\,', \chi\,']\|_\mathbb{S}^2}_{F_\mathrm{s}[\vec{w}\,', \chi\,']}\,, \tag{9}$$

where $\eta_\mathrm{d} = \||H^+|^2 - |H^{+;\mathrm{i}}|^2\|_\mathbb{D}^{-2}$ and $\eta_\mathrm{s}[\chi\,'] = \|\chi\,'\vec{E}^\mathrm{i}\|_\mathbb{S}^{-2}$ are the weights such that $F[\vec{0}, \chi\,'] \equiv 1$ with an equal contribution from the two addenda [32]. In the latter equation a data cost $F_\mathrm{d}[\vec{w}\,']$ and a state cost $F_\mathrm{s}[\vec{w}\,', \chi\,']$ are distinguished. The norms $\|\cdot\|_\mathbb{D}$ and $\|\cdot\|_\mathbb{S}$ are defined on the Hilbert spaces $\mathbb{D}$, the discrete space of the data residuals, and $\mathbb{S}$, the continuous functional space of the state residuals. In addition, it is convenient to introduce the image of the observation operator as the observation Hilbert space $\mathbb{O}$. In the following, the inner product of a generic Hilbert space $\mathbb{H}$ is denoted as $(\cdot|\cdot)_\mathbb{H}$.

3. Numerical minimisation procedure

In accordance to the traditional approach of CSI, the cost functional (9) is minimised numerically adopting a two-step alternating conjugate gradient method, which helps in dealing with the non-linearity of the problem [32].

3.1. Contrast source update

First, the contrast source is updated by applying the conjugate gradient iterative scheme

$$\vec{w}^{[n+1]} = \vec{w}^{[n]} + \alpha^{[n]}\vec{v}^{[n]}\,, \tag{10}$$

where $\alpha^{[n]}$ is the optimal real-valued step-length of the update and $\vec{v}^{[n]}$ is the Polak-Ribière direction defined iteratively as

$$\begin{cases} \vec{v}^{[0]} = \vec{0} \\ \vec{v}^{[n]} = \vec{g}^{[n]} + \dfrac{(\vec{g}^{[n]}|\vec{g}^{[n]} - \vec{g}^{[n-1]})_{\mathbb{S}}}{\|\vec{g}^{[n-1]}\|^2_{\mathbb{S}}}\vec{v}^{[n-1]}, \qquad \text{if } n \geq 1 \end{cases} \tag{11}$$

in which $\vec{g}^{[n]}$ is the gradient of the cost functional F with respect to the guess contrast source $\vec{w}\,'$ evaluated in $(\vec{w}^{[n]}, \chi^{[n]})$. The evaluation of the gradient $\vec{g}^{[n]}$ makes the contrast source update substantially different from what already described elsewhere for CSI-EPT [40]. For sake of clarity, it is convenient to split the gradient of the cost functional in two contributions $\vec{g}^{[n]} = \vec{g}_{\mathrm{d}}^{[n]} + \vec{g}_{\mathrm{s}}^{[n]}$, the gradient of the data cost $\vec{g}_{\mathrm{d}}^{[n]}$ and the one of the state cost $\vec{g}_{\mathrm{s}}^{[n]}$, respectively.

In order to compute the gradient of the data cost $\vec{g}_{\mathrm{d}}^{[n]}$, it should be interpreted as the Riesz representation of the Fréchet differential of the functional, which is conveniently indicated by the notation $\mathrm{d}_{\vec{w}}F_{\mathrm{d}}(\vec{w}^{[n]})$. Moreover, the data cost should be written exploiting the auxiliary functional f such that for any observation $u \in \mathbb{O}$, $f[u] = \||H^+|^2 - |u|^2\|^2_{\mathbb{D}}$. Thus

$$F_{\mathrm{d}}[\vec{w}\,'] = \frac{\eta_{\mathrm{d}}}{2} f[\mathcal{OS}^+_{\mathrm{h}}\vec{w}\,' + H^{+;\mathrm{i}}] \tag{12}$$

and the chain-rule can be used to evaluate the Fréchet differential leading to

$$\begin{aligned} (\vec{g}_{\mathrm{d}}^{[n]}|\vec{u})_{\mathbb{S}} = \mathrm{d}_{\vec{w}}F_{\mathrm{d}}(\vec{w}^{[n]})[\vec{u}] &= \frac{\eta_{\mathrm{d}}}{2}\mathrm{d}f(\mathcal{OS}^+_{\mathrm{h}}\vec{w}^{[n]} + H^{+;\mathrm{i}})[\mathcal{OS}^+_{\mathrm{h}}\vec{u}] \\ &= \frac{\eta_{\mathrm{d}}}{2}\left(\nabla f(\mathcal{OS}^+_{\mathrm{h}}\vec{w}^{[n]} + H^{+;\mathrm{i}})|\mathcal{OS}^+_{\mathrm{h}}\vec{u}\right)_{\mathbb{O}} \\ &= \frac{\eta_{\mathrm{d}}}{2}\left(\mathcal{S}^{+;\star}_{\mathrm{h}}\mathcal{O}^{\star}\nabla f(\mathcal{OS}^+_{\mathrm{h}}\vec{w}^{[n]} + H^{+;\mathrm{i}})|\vec{u}\right)_{\mathbb{S}}\,, \end{aligned} \tag{13}$$

for any $\vec{u} \in \mathbb{S}$. The superscript star denotes the adjoint operators. It remains to be computed the gradient of f, $\nabla f(u)$. An analitical close form can be found in a quite general context by simply assuming that the observation space is $\mathbb{O} = L^2(X;\mathbb{C})$ and the data space is $\mathbb{D} = L^2(X;\mathbb{R})$, where $(X, \Sigma, \mathfrak{m})$ is a measure space with X the set of independent variables, Σ its σ-algebra and $\mathfrak{m}$ the measure. In this case,

$$\begin{aligned} (\nabla f(u)|v)_{\mathbb{O}} &= \lim_{h\to 0}\frac{f[u+hv] - f[u]}{h} \\ &= \lim_{h\to 0}\frac{1}{h}\left(\int_X \left(|u+hv|^2 - |H^+|^2\right)^2 \mathrm{d}\mathfrak{m} - \int_X \left(|u|^2 - |H^+|^2\right)^2 \mathrm{d}\mathfrak{m}\right)\,, \end{aligned} \tag{14}$$

in which the first integral in round brackets can be elaborated noting that

$$\begin{aligned}
&\int_X \left(|u+hv|^2-|H^+|^2\right)^2 \mathrm{d}\mathfrak{m} \\
&= \int_X \left(|u|^2+h^2|v|^2+2h\mathrm{Re}(u\overline{v})-|H^+|^2\right)^2 \mathrm{d}\mathfrak{m} \\
&= \int_X \left(|u|^2-|H^+|^2\right)^2 \left(1+\frac{h^2|v|^2+2h\mathrm{Re}(u\overline{v})}{|u|^2-|H^+|^2}\right)^2 \mathrm{d}\mathfrak{m} \\
&\to \int_X \left(|u|^2-|H^+|^2\right)^2 \left(1+2\frac{h^2|v|^2+2h\mathrm{Re}(u\overline{v})}{|u|^2-|H^+|^2}\right) \mathrm{d}\mathfrak{m}, \quad \text{for } h\to 0\,.
\end{aligned} \tag{15}$$

The overline denotes the complex conjugate. By combining (14) and (15), it results that

$$\begin{aligned}
(\nabla f(u)|v)_{\mathbb{O}} &= \mathrm{Re}\int_X 4\left(|u|^2-|H^+|^2\right)u\overline{v}\mathrm{d}\mathfrak{m} \\
&= \left(4\left(|u|^2-|H^+|^2\right)u|v\right)_{\mathbb{O}}\,.
\end{aligned} \tag{16}$$

Thus, from (13) and (16) it follows that

$$\vec{g}_{\mathrm{d}}^{\,[n]} = -2\eta_{\mathrm{d}}\mathcal{S}_{\mathrm{h}}^{+;\star}\mathcal{O}^{\star}\left[\rho[\vec{w}^{\,[n]}](\mathcal{O}\mathcal{S}_{\mathrm{h}}^{+}\vec{w}^{\,[n]}+H^{+;\mathrm{i}})\right]\,. \tag{17}$$

It is worth noting that the latter relation is quite generic. It holds for the observation operator $\mathcal{O}$ defined by (5), in which case $X=\{1,\ldots,N\}$, $\mathfrak{m}$ is the counting measure and the integrals become summations. Moreover, it holds in case the observation operator is omitted and a continuous approximation of the mapped transmit sensitivity is employed setting, for instance, $X\subset\Omega$ and $\mathfrak{m}$ the Lebesgue measure.

The gradient of the state cost is computed in the same easier way described elsewhere for the CSI-EPT technique to obtain [40]

$$\vec{g}_{\mathrm{s}}^{\,[n]} = -\eta_{\mathrm{s}}[\chi^{[n]}]\left(\vec{r}\,[\vec{w}^{\,[n]},\chi^{[n]}]-\mathcal{S}_{\mathrm{e}}^{\star}\left[\overline{\chi}^{[n]}\vec{r}\,[\vec{w}^{\,[n]},\chi^{[n]}]\right]\right)\,. \tag{18}$$

Once the gradient $\vec{g}^{\,[n]}$ is obtained by summing up (17) and (18) and the update direction is determined in accordance to (11), the optimal step-length $\alpha^{[n]}$ should be computed as the real-valued minimiser of the cost function $F[\vec{w}^{\,[n]}+\alpha\vec{v}^{\,[n]},\chi^{[n]}]$. Because of the chain-rule, $\alpha^{[n]}$ solves the Euler equation

$$\mathrm{d}_{\vec{w}}F_{\mathrm{d}}(\vec{w}^{\,[n]}+\alpha\vec{v}^{\,[n]})[\vec{v}^{\,[n]}]+\mathrm{d}_{\vec{w}}F_{\mathrm{s}}(\vec{w}^{\,[n]}+\alpha\vec{v}^{\,[n]},\chi^{[n]})[\vec{v}^{\,[n]}]=0\,, \tag{19}$$

whose left-hand side is the following cubic polynomial, as can be made explicit by exploiting (17) and (18),

$$2\eta_{\mathrm{d}}\sum_{i=1}^{3}\alpha^i(A_i|\mathcal{O}\mathcal{S}_{\mathrm{h}}^{+}\vec{v}^{\,[n]})_{\mathbb{O}}+\alpha\;\eta_{\mathrm{s}}[\chi^{[n]}]\|\chi^{[n]}\mathcal{S}_{\mathrm{e}}\vec{v}^{\,[n]}-\vec{v}^{\,[n]}\|_{\mathbb{S}}^2+(\vec{g}^{\,[n]}|\vec{v}^{\,[n]})_{\mathbb{S}}\,, \tag{20}$$

with

$$A_1 = \rho[\vec{w}^{\,[n]}]\mathcal{O}\mathcal{S}_{\mathrm{h}}^{+}\vec{v}^{\,[n]}+2\mathrm{Re}\left(O^{[n]}\;\overline{\mathcal{O}\mathcal{S}_{\mathrm{h}}^{+}\vec{v}^{\,[n]}}\right)O^{[n]}\,, \tag{21}$$

$$A_2 = \left|\mathcal{O}\mathcal{S}_{\mathrm{h}}^{+}\vec{v}^{\,[n]}\right|^2 O^{[n]}+2\mathrm{Re}\left(O^{[n]}\;\overline{\mathcal{O}\mathcal{S}_{\mathrm{h}}^{+}\vec{v}^{\,[n]}}\right)\mathcal{O}\mathcal{S}_{\mathrm{h}}^{+}\vec{v}^{\,[n]}\,, \tag{22}$$

$$A_3 = \left|\mathcal{O}\mathcal{S}_{\mathrm{h}}^{+}\vec{v}^{\,[n]}\right|^2\mathcal{O}\mathcal{S}_{\mathrm{h}}^{+}\vec{v}^{\,[n]}\,, \tag{23}$$

where $O^{[n]} = (\mathcal{O}\mathcal{S}_{\mathrm{h}}^{+}\vec{w}^{\,[n]} + H^{+;\mathrm{i}})$. Therefore, equation (19) can be solved analytically and at least a real solution certainly exists. If the polynomial has three real roots, then $\alpha^{[n]}$ can be chosen amongst them by checking the minimisation of the cost function.

3.2. Contrast update

The updated contrast source $\vec{w}^{\,[n+1]}$ is used to compute the new contrast $\chi^{[n+1]}$ in the traditional approach followed by CSI [32]. Since the contrast affects only the state cost, which is not changed in CSI-GMT with respect to CSI-EPT, it is defined as the minimiser of the norm of the state residual. In this way, the dependence of the state weight $\eta_{\mathrm{s}}[\chi']$ on the contrast is overlooked and the following analitical expression is employed [40],

$$\chi^{[n+1]} = \frac{\vec{w}^{\,[n+1]} \cdot \overline{\vec{E}^{\mathrm{i}} + \mathcal{S}_{\mathrm{e}}\vec{w}^{\,[n+1]}}}{|\vec{E}^{\mathrm{i}} + \mathcal{S}_{\mathrm{e}}\vec{w}^{\,[n+1]}|^2}\,, \tag{24}$$

where the dot indicates the scalar product between vectors and the symbol $|\cdot|$ denotes the vector length.

Possible *a priori* information about the EPs distribution in the form of convex constraints can be used in contrast update by projecting the output of (24) in the convex space of admissible contrasts [32]. A classic example of such a constraint is the verification that EPs are greater or equal than the corresponding property of vacuum. If vacuum is used as background (*i.e.*, $\tilde{\varepsilon}_{\mathrm{b}} = \varepsilon_0$), then this constraint is verified by all and only the distributions with non-negative real part and non-positive imaginary part. In this case, the projection of $\chi^{[n+1]}$ in this set is performed by setting to zero the negative real parts and the positive imaginary parts in each point of the domain. Another useful *a priori* information is the knowledge of the volume occupied by the examined body, deduced from the lack of MRI signal in air. Thus, the measurements directly determine the region of air, in which, using the vacuum as background, the contrast should be null. The projection of $\chi^{[n+1]}$ in the convex set of contrasts that are null in a given region is simply achieved by setting the contrast to zero in that region [40].

3.3. Initial guess

The choice of the initial guess for the iterative minimisation procedure is a critical task, because the convergence of a local optimisation technique towards the global minimum of a non-convex functional could be strongly affected by the initial guess. Clearly, since (24) does not use the previous value of the contrast, only the contrast source requires an initial guess.

The common choice in CSI methods is the back propagation solution [32]. Unfortunately, it requires the knowledge of the whole transmit sensitivity [40] and so it cannot be employed in CSI-GMT. The possibility to set an arbitrary constant phase to the transmit sensitivity in order to compute the traditional back propagation solution has been proposed in [33]. Anyway, there are no indications about the value that should

be assigned to such a constant phase. Because of the lack of ground of this approach, it is not further investigated in this paper.

A more significant approach looks at the expected physics of the problem [45]. Since the contrast source is defined as $\vec{w} = \chi\vec{E}$, the initial guess can be found with a guess for the contrast and the electric field. The former can be assumed constant and equal to the expected averaged value of the contrast, which could be provided by anatomical considerations on the imaged body. For a more accurate guess, it is possible to distinguish between the points in air and the points in the body. The latter can be assumed equal to the incident electric field. The resulting initial guess is

$$\vec{w}^{\,[0]} = \chi^{[-1]}\vec{E}^{\,\mathrm{i}}\,, \tag{25}$$

where $\chi^{[-1]}$ denotes the contrast guess. This method for choosing the initial guess is referred in the following as D'Urso's solution. The main drawback of this strategy is that the exploited *a priori* information are limited to the expected averaged contrast and the region occupied by the body, without using the measured transmit sensitivity magnitude [45].

In order to make a complete use of the magnitude of the transmit sensitivity in the choice of the initial guess, a phaseless back propagation (PBP) solution is proposed here as a more informative alternative. According to [39], the back propagation solution is obtained by minimising the data cost $F_{\mathrm{d}}[\vec{w}\,']$ along the direction of the gradient, starting from a null contrast source. So, in other words, one step of the steepest-descent method is performed to achieve the initial guess. The same procedure can be applied for the phaseless data cost, leading to the PBP solution. For convenience of notation, let be $\vec{w}^{\,[-1]} \equiv \vec{0}$, then the steepest-descent implies that the PBP solution is defined by relation

$$\vec{w}^{\,[0]} = -\beta_0\vec{g}_{\mathrm{d}}^{\,[-1]}\,, \tag{26}$$

where, from (17), it is known that

$$\vec{g}_{\mathrm{d}}^{\,[-1]} = -2\eta_{\mathrm{d}}\mathcal{S}_{\mathrm{h}}^{+;\star}\mathcal{O}^{\star}\left[\left(|H^{+;\mathrm{i}}|^2 - |H^{+}|^2\right)H^{+;\mathrm{i}}\right]\,, \tag{27}$$

and the optimal step-length β_0 is chosen as the real minimiser of the cost function $F_{\mathrm{d}}[-\beta_0\vec{g}_{\mathrm{d}}^{\,[-1]}]$. Using the chain-rule, β_0 solves the Euler equation

$$\mathrm{d}_{\vec{w}}F_{\mathrm{d}}(-\beta_0\vec{g}^{\,[-1]})[\vec{g}^{\,[-1]}] = 0\,, \tag{28}$$

whose left-hand side is the following cubic polynomial, as can be made explicit by (17),

$$\beta_0^3\; 2\|A\|_{\mathbb{D}}^2 - \beta_0^2\; 3\,(A|B)_{\mathbb{D}} + \beta_0\left(\|B\|_{\mathbb{D}}^2 - 2\,(A|C)_{\mathbb{D}}\right) + (B|C)_{\mathbb{D}}\,, \tag{29}$$

with

$$A = |\mathcal{O}\mathcal{S}_{\mathrm{h}}^{+}\vec{g}^{\,[-1]}|^2\,, \tag{30}$$

$$B = 2\mathrm{Re}\left(H^{+;\mathrm{i}}\;\overline{\mathcal{O}\mathcal{S}_{\mathrm{h}}^{+}\vec{g}^{\,[-1]}}\right)\,, \tag{31}$$

$$C = |H^{+}|^2 - |H^{+;\mathrm{i}}|^2\,. \tag{32}$$

Therefore, the step-length β_0 can be computed analytically. Equation (28) has at least a real solution. In case the polynomial has three real roots, then β_0 can be chosen amongst them by checking the minimisation of the cost function.

The main advantages of the PBP solution with respect to other strategies for choosing the initial guess are the complete exploitation of the *a priori* information collected in the transmit sensitivity magnitude measurement and the possibility to automate the choice of the initial guess without the need of a human intervention—like, for instance, in the selection of the expected contrast.

4. Extension to multiple transmit sensitivities

The proposed CSI-GMT method can be readily extended to the case in which multiple measurements of different transmit sensitivities are provided. This is a common case when multi-channel transmit coils are employed, typically for MRI parallel transmission, which would strongly benefit of a technique for patient-specific local SAR estimation [46].

It is possible to incorporate J measurements in CSI-GMT by summing up their contributions in the cost functional, which is rewritten as [20, 35]

$$F\left[(\vec{w}_j\,')_{j=1}^{J},\chi'\right]=\frac{\eta_{\mathrm{d}}}{2}\sum_{j=1}^{J}\|\rho_j[\vec{w}_j\,']\|_{\mathbb{D}}^2+\frac{\eta_{\mathrm{s}}[\chi']}{2}\sum_{j=1}^{J}\|\vec{r}_j[\vec{w}_j\,',\chi']\|_{\mathbb{S}}^2\,, \tag{33}$$

with

$$\eta_{\mathrm{d}}=\left(\sum_{j=1}^{J}\||H_j^+|^2-|H_j^{+;\mathrm{i}}|^2\|_{\mathbb{D}}^2\right)^{-1}, \tag{34}$$

$$\eta_{\mathrm{s}}[\chi']=\left(\sum_{j=1}^{J}\|\chi'\vec{E}_j^{\mathrm{i}}\|_{\mathbb{S}}^2\right)^{-1}. \tag{35}$$

The subscript j denotes the j-th coil setting, with its own incident field $\{\vec{E}_j^{\mathrm{i}},\vec{B}_j^{\mathrm{i}}\}$, measured transmit sensitivity magnitude $|B_{1,j}^+|^2$ and contrast source $\vec{w}_j$. The j-th data and state residuals are defined accordingly. It is worth noting that, although the contrast source depends on the setting, the contrast is common to all the measurements.

The update of the J contrast sources is performed in a single step according to the scheme [35]

$$\vec{w}_j^{[n+1]}=\vec{w}_j^{[n]}+\alpha^{[n]}\vec{v}_j^{[n]}\,, \tag{36}$$

where the Polak-Ribière direction $\vec{v}_j^{[n]}$ is defined by (11) with the gradient of the cost function computed with respect to the j-th contrast source guess. Consequently, the common optimal step-length $\alpha^{[n]}$ is chosen between the real roots of the cubic polynomial obtained by summing up the polynomials (20) associated to each coil setting. Then, the contrast is updated as the minimiser of the sum of the squared state residuals norms, namely [35]

$$\chi^{[n+1]}=\frac{\sum_{j=1}^{J}\vec{w}_j^{[n+1]}\cdot\overline{\vec{E}_j^{\mathrm{i}}+\mathcal{S}_{\mathrm{e}}\vec{w}_j^{[n+1]}}}{\sum_{j=1}^{J}|\vec{E}_j^{\mathrm{i}}+\mathcal{S}_{\mathrm{e}}\vec{w}_j^{[n+1]}|^2}\,. \tag{37}$$

Lastly, the initial guess is chosen applying D'Urso's or the PBP solutions independently to each coil setting.

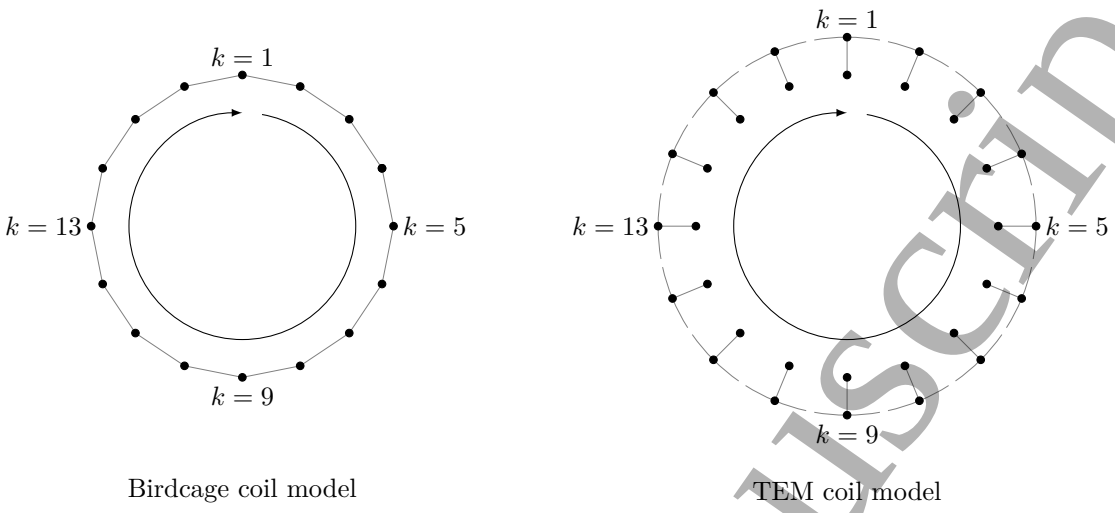

Figure 1. Diagrammatic representation of a 16-legs quadrature birdcage coil and a TEM coil. The black dots denote the locations of line sources, whereas the grey lines indicate the implicit connections between the conductors. The sources are numbered clockwise by the index k.

The functional point of view used in this paper allows to figure out very easily the extension of CSI-GMT to multiple measurements by carrying out the minimisation in the direct sum spaces $\mathbb{D}^J$ and $\mathbb{S}^J$, with the naturally induced inner products.

5. Results and discussion

In this section, the feasibility of performing MREPT using the proposed technique is verified by its application to two-dimensional model problems mimicking sections of an anatomical human body.

The mid-planes of 16-legs quadrature birdcage coils and of TEM coils with 4, 8, and 16 legs are modelled in a boundary-free domain using the transverse magnetic (TM) assumption (*i.e.*, $H_z = 0$, $E_x = E_y = 0$), which allows handling the models as two-dimensional ones. In particular, the legs of the birdcage coils are modelled as line sources uniformly distributed on a circumference of radius R (cf. figure 1). If the line sources are numbered clockwise by the index $k = 1, \ldots, 16$, the current with unitary intensity in the k-th leg is

$$I_k^{\mathrm{BC}} = \mathrm{e}^{\mathrm{i}\pi k/8}, \tag{38}$$

such that an almost positively rotating magnetic field is generated within the birdcage when the coil is unloaded. In order to model the TEM coils, the line sources are uniformly distributed with the same angular positions on a couple of concentric circumferences, one with radius R and the other with radius $R + \Delta R$, using $\Delta R = 2\,\mathrm{cm}$ (cf. figure 1). The larger circumference models the segmented conductive shield which acts as returning lines [47]. Despite TEM coils are often driven in quadrature like birdcage coils, they can be driven with as many independent excitations as the number

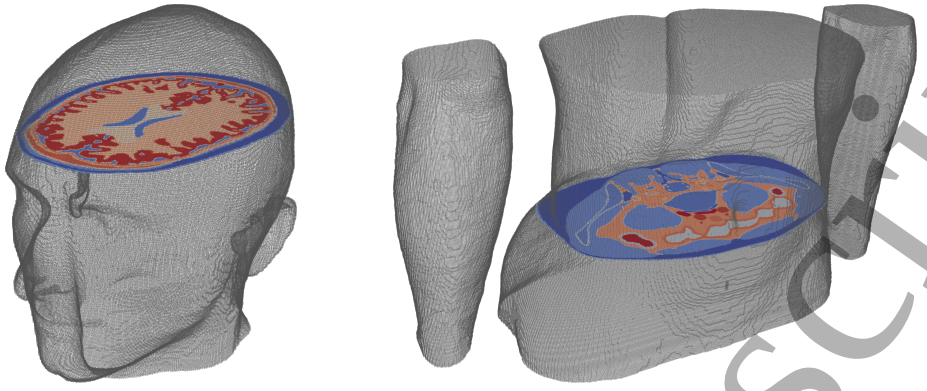

Figure 2. Sections of the head (left) and the abdomen (right) of the anatomical human model Duke from the Virtual Family [48] used in the realistic model problems. The colours in the sections denote different biological tissues.

of legs and so be used as multi-channel transmit coils. In the following, if J legs are numbered clockwise by the index $k = 1, \ldots, J$, the currents of unitary intensity imposed by the j-th excitation in the inner circumference are described by the relation

$$I_k^{\mathrm{TEM},j} = \delta_{j,k} \mathrm{e}^{\mathrm{i}2\pi k/J} \,, \tag{39}$$

where $\delta_{j,k}$ is the Kronecker delta , equal to one when $j = k$ and to zero otherwise. On the other hand, the current of the k-th line in the outer circle is $-I_k^{\mathrm{TEM},j}$. Thus, each excitation involves only a couple of line sources, one for each circumference, having the same angular position.

The TM assumption is maintained when modelling a loaded coil, so just a section of the imaged body is considered. In the following, both a section of the head and a section of the abdomen of the anatomical human model Duke from the Virtual Family [48] are studied (figure 2), because of their very different geometrical structures and electric properties. The electric properties of the biological tissues are defined by the 4^{th} order Cole-Cole dispersive model [49] applied to the measurements collected in the IT'IS foundation database [50]. In this context, air is assumed as the background ($\tilde{\varepsilon}_{\mathrm{b}} \equiv \varepsilon_0$) and the incident and the total electromagnetic fields generated by the transmit coils at 128 MHz (the operative frequency for 3 T scanners) are simulated numerically by the method of moments applied on 1 mm Cartesian grids. The obtained fields are used as noise-free virtual measurements for CSI-GMT, which still requires a specialisation of the operators $\mathcal{S}_{\mathrm{e}}$ and $\mathcal{S}_{\mathrm{h}}$ for the particular case.

The maps recovered by CSI-GMT are quantitatively compared with the expected ones by the global relative error

$$\mathrm{RE}[m] = \sqrt{\frac{\sum_{i=1}^{N_{\mathrm{px}}} (m_i - m_i^*)^2}{\sum_{i=1}^{N_{\mathrm{px}}} m_i^{*2}}} \,, \tag{40}$$

and the correlation coefficient

$$\mathrm{CC}[m] = \frac{\sum_{i=1}^{N_{\mathrm{px}}} m_i m_i^*}{\sqrt{\sum_{i=1}^{N_{\mathrm{px}}} m_i^2} \sqrt{\sum_{i=1}^{N_{\mathrm{px}}} m_i^{*2}}} \,, \tag{41}$$

where $(m_i)_{i=1}^{N_{\mathrm{px}}}$ denotes the generic recovered quantities in the N_{px} pixels inside the imaged body and $(m_i^*)_{i=1}^{N_{\mathrm{px}}}$ denotes the corresponding expected quantities. The analysis is performed on recovered relative permittivity $\varepsilon_{\mathrm{r}} = \varepsilon/\varepsilon_0$ and electric conductivity σ.

5.1. Operators implementation

The operators introduced in the functional framework for CSI-GMT must be specialised and implemented coherently with the physics of the used RF coils.

In the cases considered here, since the presence of RF shields around the coils has been neglected, Maxwell's equations (2) can be solved semi-analytically in a homogeneous boundary-free domain by convolution products of the dyadic Green's functions with the equivalent scattering current [42]. Thus,

$$\left(\mathcal{S}_{\mathrm{e}}\vec{w}\right)(\vec{p}) = \int_{\Omega} \left(\left(\nabla\nabla + \kappa_{\mathrm{b}}^2\mathcal{I}\right)\psi(\vec{p}-\vec{q})\right)\vec{w}(\vec{q})\,\mathrm{d}\vec{q}, \tag{42}$$

and

$$\left(\mathcal{S}_{\mathrm{h}}\vec{w}\right)(\vec{p}) = \int_{\Omega} \mathrm{i}\omega\tilde{\varepsilon}_{\mathrm{b}}\nabla\psi(\vec{p}-\vec{q}) \times \vec{w}(\vec{q})\,\mathrm{d}\vec{q}, \tag{43}$$

where $\kappa_{\mathrm{b}} = \omega\sqrt{\tilde{\varepsilon}_{\mathrm{b}}\mu_0}$ is the propagation coefficient of the radiation, $\mathcal{I}$ is the identity operator and ψ is the fundamental solution of the Helmholtz equation with propagation coefficient κ_{b}. In two dimensions, $\psi(\vec{p}-\vec{q}) = -\mathrm{i}H_0^{(2)}(\kappa_{\mathrm{b}}|\vec{p}-\vec{q}|)/4$ with $H_0^{(2)}$ denoting the zeroth order Hankel function of the second kind. In other situations, more suitable operators may be introduced [40].

The adjoint operators are consequently obtained by defining $\mathbb{S} = L^2(\Omega)$, $\mathbb{D} = \mathbb{R}^N$ and $\mathbb{O} = \mathbb{C}^N$, with N the number of measurement points, and assuming that all the involved fields belong to $L^2(\Omega)$. Precisely, $\mathcal{S}_{\mathrm{e}}^\star$ and $\mathcal{S}_{\mathrm{h}}^\star$ are the correlation products of the conjugate transpose of the dyadic Green's functions with the input field [40],

$$\left(\mathcal{S}_{\mathrm{e}}^\star\vec{v}\right)(\vec{p}) = \int_{\Omega} \left(\left(\nabla\nabla + \overline{\kappa}_{\mathrm{b}}^2\mathcal{I}\right)\overline{\psi}(\vec{q}-\vec{p})\right)\vec{v}(\vec{q})\,\mathrm{d}\vec{q}, \tag{44}$$

and

$$\left(\mathcal{S}_{\mathrm{h}}^\star\vec{v}\right)(\vec{p}) = \int_{\Omega} \mathrm{i}\omega\overline{\tilde{\varepsilon}}_{\mathrm{b}}\nabla\overline{\psi}(\vec{q}-\vec{p}) \times \vec{v}(\vec{q})\,\mathrm{d}\vec{q}. \tag{45}$$

All these integral operators are implemented numerically in a very efficient way by using the fast Fourier transform (FFT) algorithm. The results collected in this section have been obtained with a homemade C++ code exploiting the FFTW 3.3.4 library [51] for FFT computations.

Moreover, it is worth noting that the dual of the observation operator $\mathcal{O}$ defined by (5) is, for any ordered set $v = (v_i)_{i=1}^N$,

$$\mathcal{O}^\star v = \sum_{i=1}^{N} v_i\delta_{\vec{p}_i}\,, \tag{46}$$

being $\delta_{\vec{p}_i}$ the Dirac delta centred in $\vec{p}_i$ and $(\vec{p}_i)_{i=1}^N$ the set of the measurement points. Similarly, $\mathcal{S}_{\mathrm{h}}^{+;\star} = \mathcal{S}_{\mathrm{h}}^\star\mathcal{P}^\star$ and, for any scalar field v,

$$\mathcal{P}^\star v = \frac{v}{2}\left(\hat{x} - \mathrm{i}\hat{y}\right)\,. \tag{47}$$

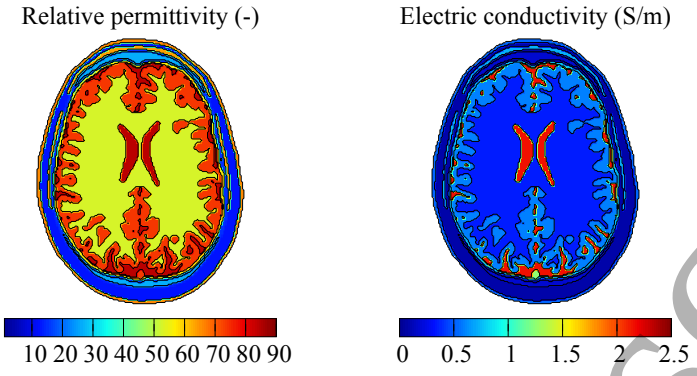

Figure 3. EPs assigned to the tissues of the considered head section. The tissues' boundaries are drawn with black lines.

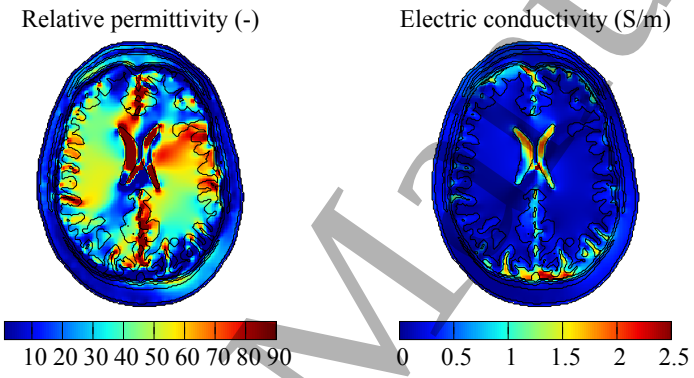

Figure 4. EPs distributions of the head section recovered by CSI-GMT after 1000 iterative steps with input fields generated by a quadrature birdcage coil. PBP solution is used as initial guess. The actual tissues' boundaries are drawn with black lines. To be compared with the actual EPs spatial distributions in figure 3.

5.2. Imaging of the head's properties

The EPs assigned to each tissue of the considered section of the head are reported in figure 3, where the boundaries between different tissues are highlighted. CSI-GMT is used to recover these maps starting from virtual measurements of the incident fields and of the transmit sensitivities magnitudes generated by coils with inner radius $R = 14\,\mathrm{cm}$. The PBP solution has been tested as initial guess by comparing its results with those obtained using D'Urso's solution, with $\chi^{[0]}$ null in pixels outside the head and equal to the contrast of the white matter ($\varepsilon_\mathrm{r} = 52.5$ and $\sigma = 0.34\,\mathrm{S\,m^{-1}}$), which is the largest tissue in the section, in the inner pixels.

The lack of phase information strongly affects the recovery when just one measurement is used, like in the case of a quadrature birdcage coil in transmission. Figure 4 shows the EPs obtained by 1000 iterative steps of CSI-GMT starting from the PBP solution in this situation. After 1000 iterative steps the decreasing rate of the cost functional is very small, suggesting that convergence is reached, but the global relative errors in the recovered maps are still high, as can be appreciated in figure 5. On the other hand, the correlation coefficients reported in figure 5 suggest partial reproduction

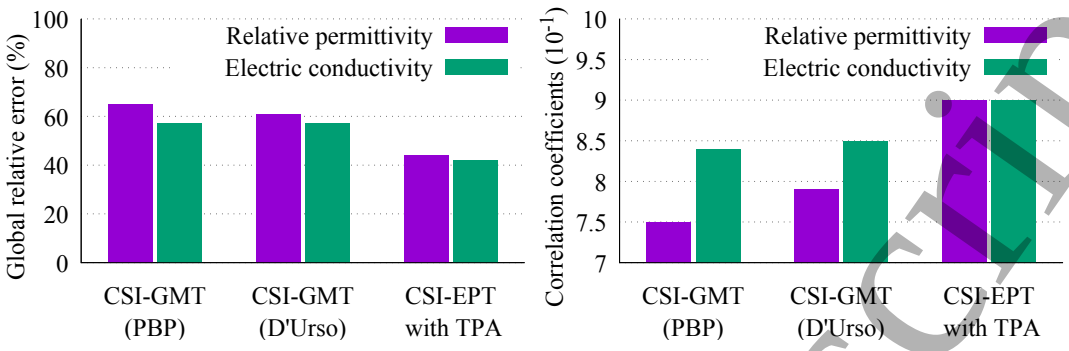

Figure 5. Global relative errors and correlation coefficients of the maps of EPs of the head section recovered by CSI-GMT, with both the considered initial guesses, and CSI-EPT, using the TPA, after 1000 iterative steps using as input data the measurements provided by a quadrature birdcage coil.

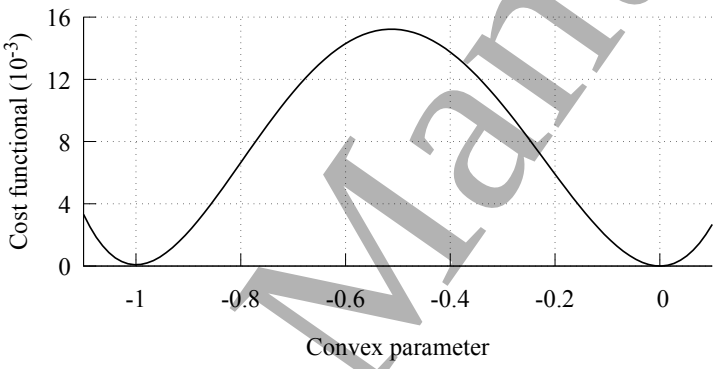

Figure 6. Trend of the cost functional on the line joining the actual solution $(\vec{w}, \chi)$ to the point reached by CSI-GMT after 1000 steps starting from the PBP solution when input fields are provided by a quadrature birdcage coil in presence of the head section. The convex parameter is such that zero corresponds to the actual solution, whereas -1 corresponds to the recovered minimum.

of the expected pattern just for the electric conductivity. Actually, at the considered iteration, the minimisation procedure has already reached convergence, but it has got stuck in a local minimum of the cost functional, as can be deduced from figure 6, in which the cost functional on the line joining the recovered solution to the expected distributions is plotted. A completely analogous result is obtained also with the other initial guess.

In a 3 T scanner, the adoption of a quadrature birdcage coil both in transmission and in reception with a polarisation switch between the two behaviours is, however, a particular choice that allows the estimation of B_1^+ phase by means of the so-called transceive phase assumption (TPA) [25]. The maps obtained by CSI-EPT after 1000 steps using as input the complex transmit sensitivity estimated with the TPA are reported in figure 7. The error introduced in this case is significantly less than that introduced by CSI-GMT and can be quantified by the global relative errors and the correlation coefficients of both relative permittivity and electric conductivity reported

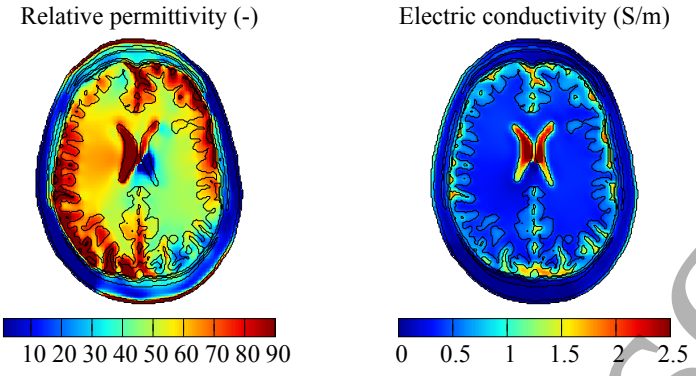

Figure 7. EPs distributions of the head section recovered by CSI-EPT after 1000 iterative steps with input fields generated by a quadrature birdcage coil with the TPA. The actual tissues' boundaries are drawn with black lines. To be compared with the actual EPs spatial distributions in figure 3.

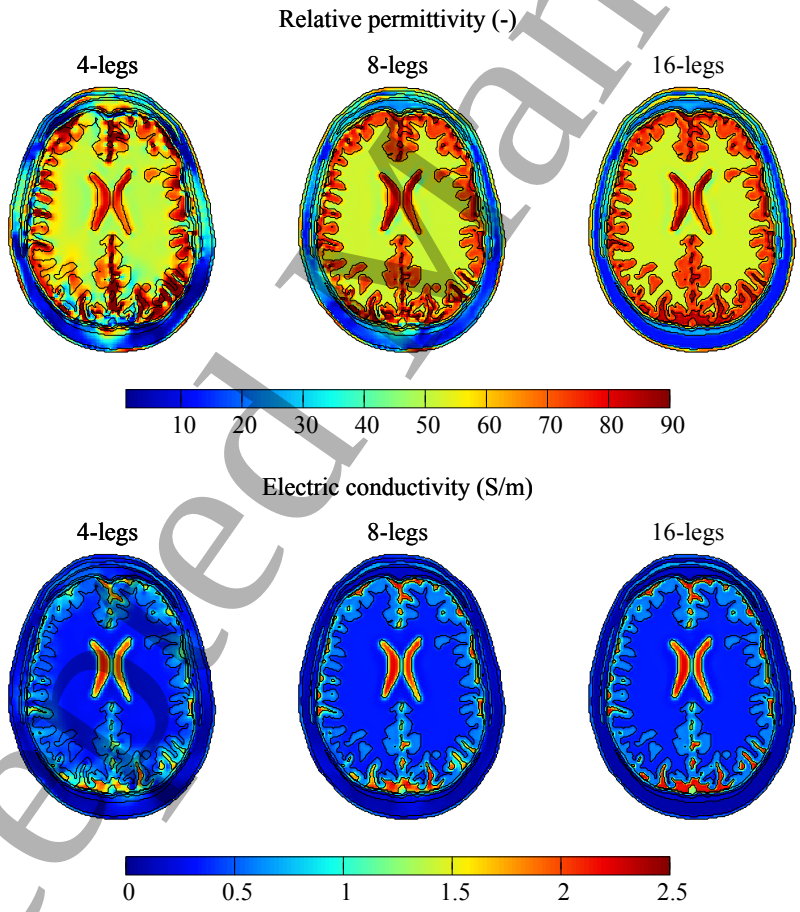

Figure 8. EPs distributions of the head section recovered by CSI-GMT after 1000 iterative steps with input fields generated by 4, 8, and 16-legs TEM coils. Phaseless back propagation is used as initial guess. The actual tissues' boundaries are drawn with black lines. To be compared with the actual EPs spatial distributions in figure 3.

in figure 5.

The quality of the images recovered by CSI-GMT improves when multiple inputs

Table 1. Global relative errors and correlation coefficients of the maps of the head section recovered by CSI-GMT after 1000 iterative steps with input fields provided by 4, 8, and 16-legs TEM coils. Results obtained with both the initial guesses are reported.

	PBP solution				D'Urso's solution			
	ER[ε_r]	CC[ε_r]	ER[σ]	CC[σ]	ER[ε_r]	CC[ε_r]	ER[σ]	CC[σ]
4-legs	33 %	0.94	37 %	0.93	35 %	0.93	37 %	0.93
8-legs	20 %	0.97	27 %	0.96	20 %	0.97	26 %	0.96
16-legs	13 %	0.99	24 %	0.97	14 %	0.99	24 %	0.96

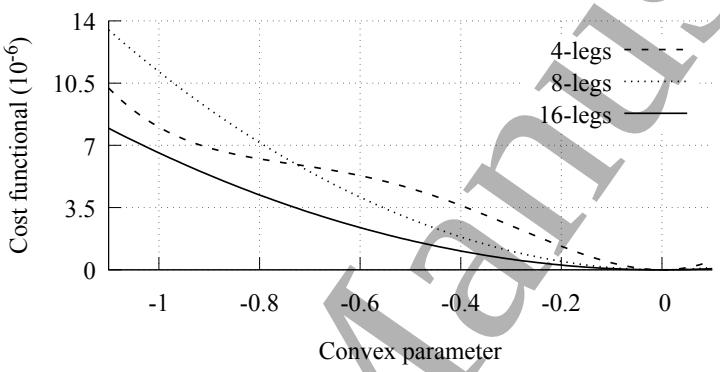

Figure 9. Trend of the cost functional on the lines joining the actual solution $(\vec{w}, \chi)$ to the points reached by CSI-GMT after 1000 steps starting from the PBP solution when input fields are provided by a 4, 8, and 16-legs TEM coil simulated in presence of the head section. The convex parameter is such that zero corresponds to the actual solution, whereas -1 corresponds to the estimated minima.

are provided, like in the case of TEM coils used as multi-channel transmit coils. In passing, in this situation there is not an easy way to estimate the phases of the transmit sensitivities, so CSI-EPT cannot be used as an alternative. The maps of EPs estimated by CSI-GMT after 1000 iterative steps starting from PBP solution are collected in figure 8, where the results achieved by simulating 4, 8, and 16-legs TEM coils are compared. According to [47], it is technologically admissible to build TEM head coils with up to 16 legs, so the presented analysis studies up to the maximum number of measurements that would be available in a realistic arrangement. Tissues' pattern is satisfactorily reproduced when CSI-GMT receives just 4 inputs, but it gets more accurate when more independent fields are provided as inputs. A quantitative corroboration of this fact is given by table 1, where the global relative errors and the correlation coefficients are reported for both the EPs. Moreover, table 1 shows that the choice between the two initial guesses does not affect significantly the iterative procedure. Going on with the iterative steps, CSI-GMT gets stuck in a local minimum of the cost functional when measurements from the 4-legs TEM coil are used. Thus, the global relative error does not decrease further in that case. On the other hand, when 8 or more legs are considered as independent channels, the method converges to

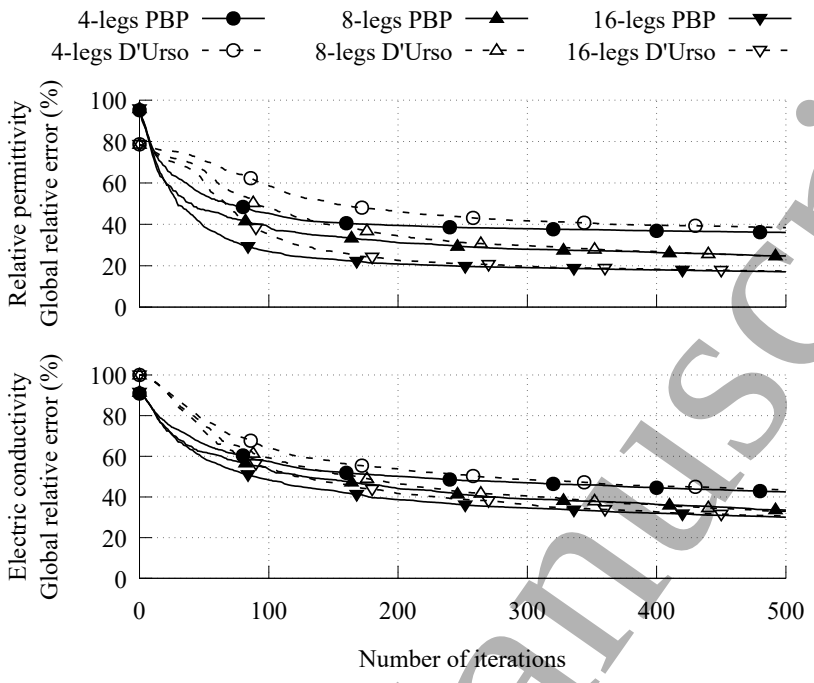

Figure 10. Trend of the global relative errors of the recovered EPs in the head section against the iterative step when input fields are provided by a 4, 8, and 16-legs TEM coil. Both PBP and D'Urso's solutions have been used as initial guess.

the expected distributions. Looking at the trends of the cost functional along the lines joining the recovered solutions after 1000 steps to the expected distributions (figure 9), the presence of the local minimum can be guessed for the 4-legs case because of the existence of two inflexion points, which would degenerate in the occurrence of a local minimum after a certain number of iterations.

Despite the two initial conditions lead to almost the same images after enough iterative steps, the choice of the initial guess affects considerably the first steps of the minimisation procedure. As can be seen in figure 10, for all the considered TEM coils, the error in the EPs estimated starting from the PBP solution is less than the error in the EPs obtained starting from D'Urso's solution up to about 300 steps. Particularly, in the very first steps, the decreasing rate is significantly higher when the PBP solution is used. This observation confirms that the PBP solution is a more informative initial guess than D'Urso's solution.

In order to prove the robustness of CSI-GMT and, consequently, the generality of the discussed results, the method has been challenged by corrupting the simulated transmit sensitivities with an additive Gaussian noise with null mean and variance equal to 2 % and 5 % of the spatially averaged $|B_{1,j}^{+}|^2$. Moreover, the minimisation has been performed on a different grid (with 2 mm sides) with respect to the one used for the direct problem, so that the *inverse crime* has not been committed. The incident field, instead, has been used noise-free assuming that the uncertainty in coil characterisation is less relevant than that in *in vivo* measurements [35]. The results obtained after 200 iterative steps of CSI-GMT starting from the PBP solution are collected in figure 11

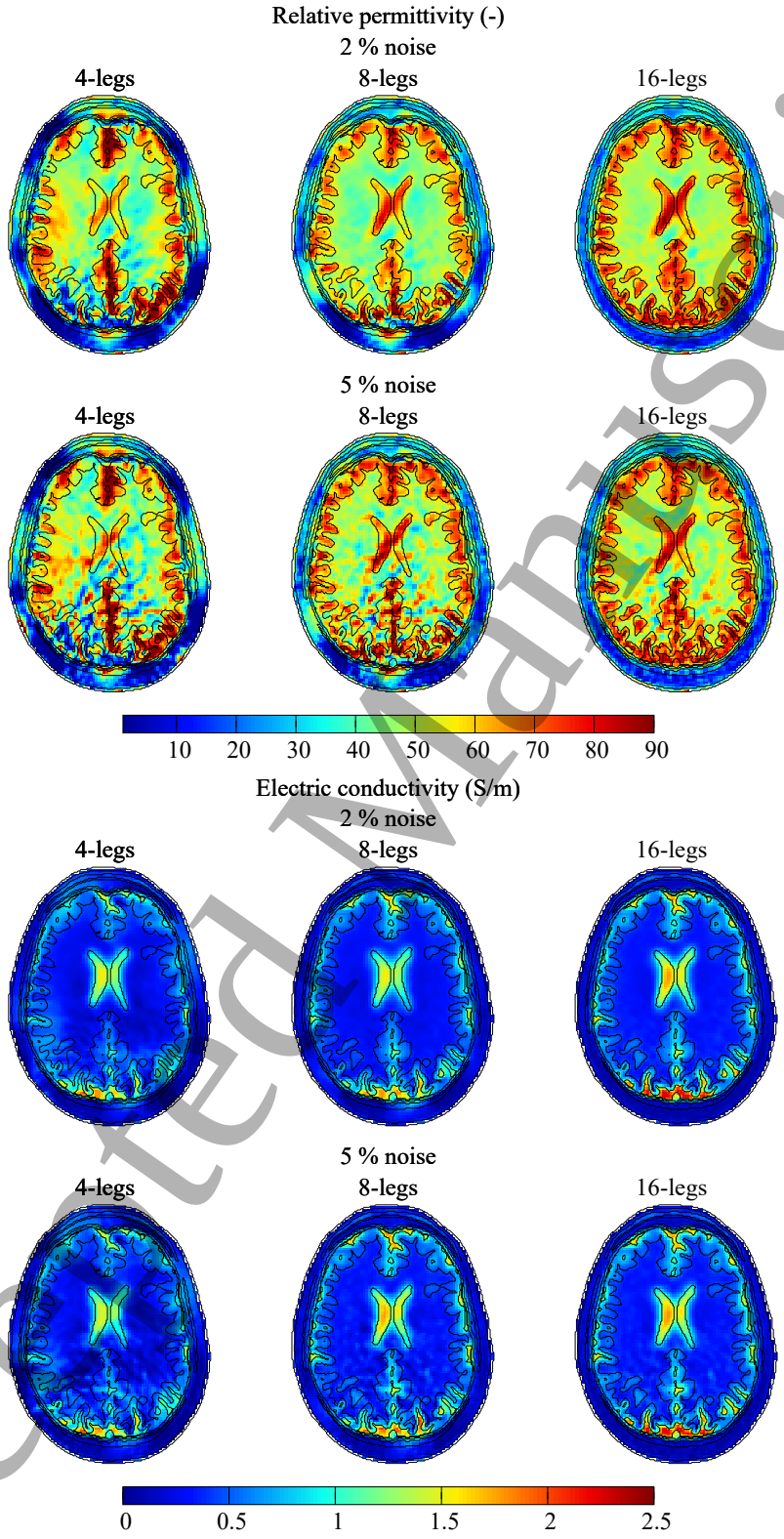

Figure 11. EPs distributions of the head section recovered on a 2 mm grid by CSI-GMT after 200 iterative steps with input generated by 4, 8, and 16-legs TEM coils and corrupted by 2 % and 5 % noise. The PBP solution is used as initial guess.

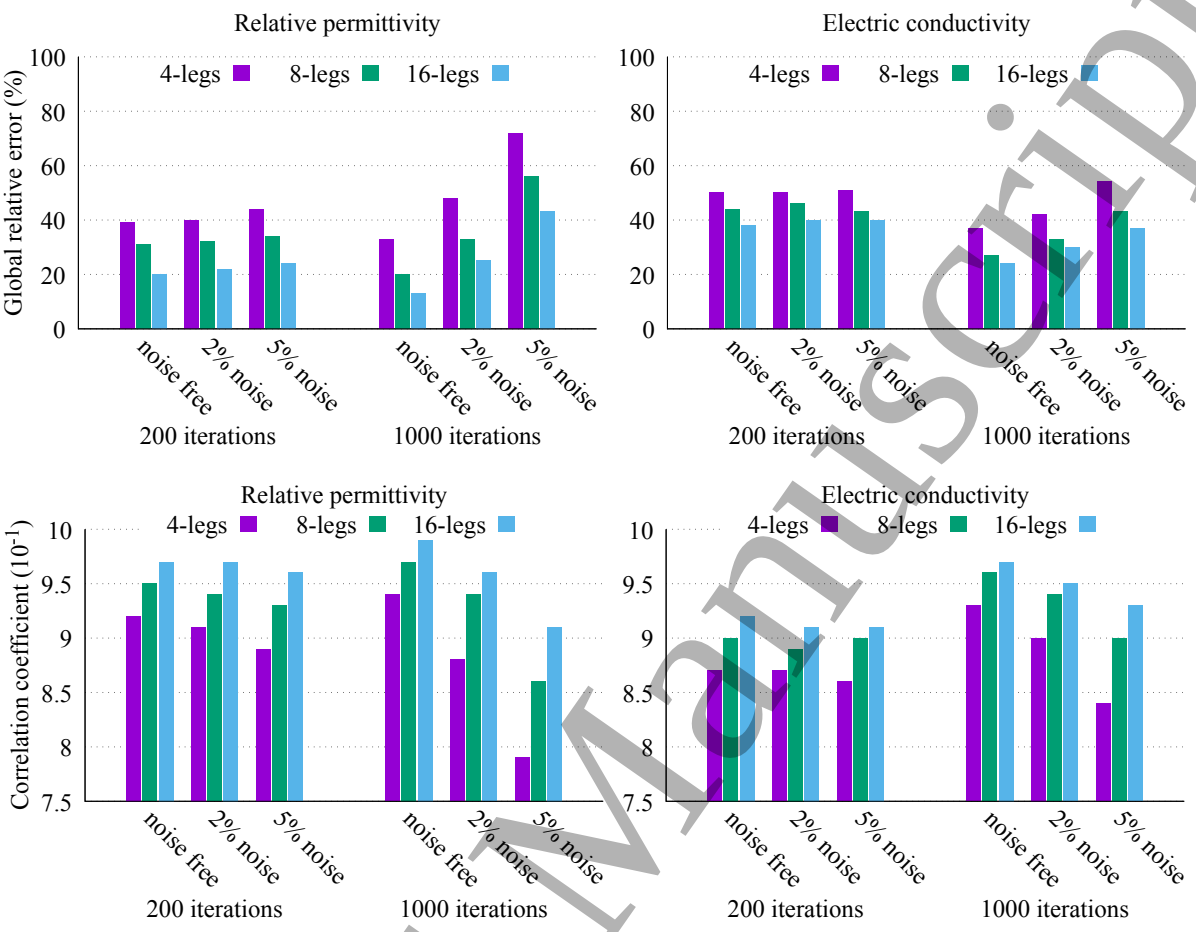

Figure 12. Global relative errors and correlation coefficients of the maps of EPs of the head section recovered on a 2 mm grid by CSI-GMT after 200 and 1000 iterative steps with input fields generated by 4, 8, and 16-legs TEM coils. Noise-free inputs are considered as well as inputs corrupted by 2 % and 5 % noise. The PBP solution is used as initial guess.

for both the amounts of noise. Despite the presence of noise and the early stop of the iterative procedure, the level of detail of the obtained maps is comparable to that of the distributions reported in figure 8. Moreover, the distributions achieved with the higher amount of noise are very similar to those obtained with the 2 % noise, both for the electric conductivity and, when 16 measurements are provided, for the relative permittivity. The observed robustness of the method is a consequence of the early stop of the iterative procedure, which acts like a regularisation strategy.

Quantitatively, figure 12 reports the global relative errors and the correlation coefficients in the EPs maps recovered by CSI-GMT after 200 and 1000 iterative steps when the input is noise-free or corrupted by 2 % or 5 % noise. The results are collected using the PBP solution as initial guess, but they are analogous when D'Urso's solution is used instead. As already seen in figure 11, it appears that the adoption of an early stop after 200 iterative steps leads to an almost noise independent recovery of the EPs distributions. On the other hand, by going on with the numerical minimisation up

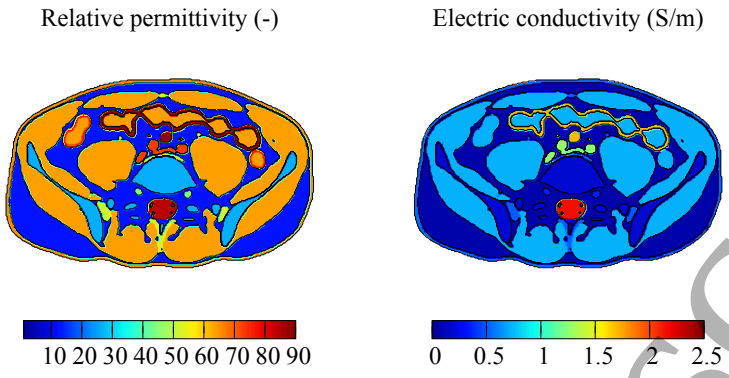

Figure 13. EPs assigned to the tissues of the considered abdomen section. The tissues' boundaries are drawn with black lines.

to 1000 iterations, the noise in input data significantly affects the results leading to an increase of the global relative errors and to a decrease of the correlation coefficients when higher amount of noise are introduced. It is worth noting that, according to both the global relative error and the correlation coefficient, the quality of the maps of relative permittivity recovered after 1000 iterations is worse than that of the maps obtained after 200 iterations in the noisy cases, whereas the electric conductivity would be better estimated after 1000 iterations even when 5% noise is considered. Summing up, as already shown for CSI-EPT [35], when multiple measurements are provided an early stop in the iterative minimisation could efficiently replace the adoption of a regularisation term in the cost functional.

5.3. Imaging of the abdomen's properties

Virtual measurements of the incident fields and of the transmit sensitivities magnitudes generated by coils with inner radius $R = 35\,\mathrm{cm}$ are used by CSI-GMT to recover the maps of the EPs reported in figure 13. As well as the PBP, also D'Urso's solution has been used as initial condition by imposing $\chi^{[0]}$ null in pixels outside the body and equal to the contrast of the muscle ($\varepsilon_\mathrm{r} = 63.5$ and $\sigma = 0.72\,\mathrm{S\,m^{-1}}$), the largest tissue in the section, in the inner pixels.

As already seen for the head section, the use of a single measurement provided by a quadrature birdcage coil is not enough to retrieve the EPs satisfactorily. Independently of the chosen initial guess, the numerical minimisation gets stuck in a local minimum of the cost functional which is far from the excepted distributions.

The results of CSI-GMT strongly improve when multiple inputs provided by multi-channel TEM coils are used. For the abdomen section, four measurements are enough to reach the global minimum of the cost functional. Anyway, in this case the initial guess affects significantly the EPs recovery. Precisely, with the inputs provided by the 8-legs TEM coil, the convergence of CSI-GMT starting from D'Urso's solution is extremely slow to the extent that after 1000 steps the method seems stuck in a local minimum, although after about 2000 steps it would reach the expected distributions. On the other

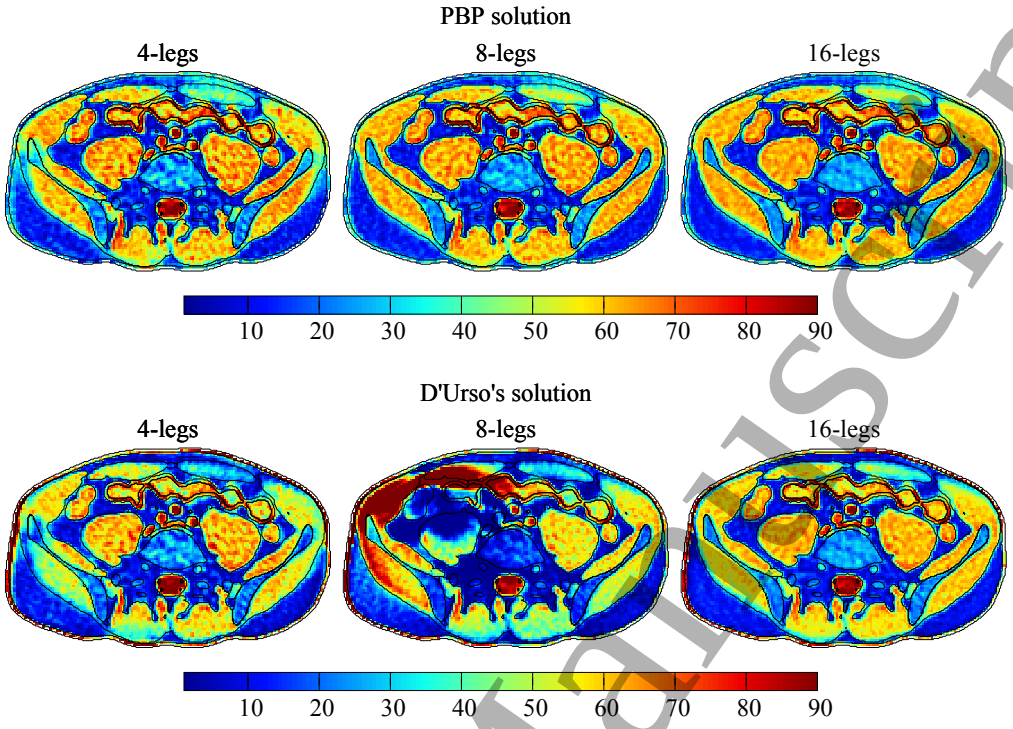

Figure 14. Relative permittivity distributions of the abdomen section recovered on a 2 mm grid by CSI-GMT after 1000 iterative steps with noisy input fields generated by 4, 8, and 16-legs TEM coils. The input transmit sensitivity is corrupted by an additive Gaussian noise with variance equal to 2 % of the spatially averaged $|B_{1,j}^{+}|^2$, whereas the incident field is known exactly. The actual tissues' boundaries are drawn with black lines. To be compared with the actual EPs spatial distributions in figure 13.

hand, the use of the PBP solution as initial guess always leads near the global minimum of the cost functional within 1000 iterative steps.

The sensitivity of the method with respect to the initial condition is clear in figure 14, where the maps of the relative permittivity estimated on a 2 mm grid after 1000 steps of CSI-GMT with noisy inputs are collected. A Gaussian noise with variance equal to 2 % of the spatially averaged $|B_{1,j}^{+}|^2$ is added to the simulated transmit sensitivities. The incident fields, on the other hand, are assumed to be known exactly. Probably, the bad performance of D'Urso's solution in this situation is due to the presence of a significant portion of fat ($\varepsilon_r = 12.4$ and $\sigma = 0.07\,\mathrm{S\,m^{-1}}$), whose EPs are very different to the ones of muscle ($\varepsilon_r = 63.5$ and $\sigma = 0.72\,\mathrm{S\,m^{-1}}$), making the choice of the homogeneous contrast $\chi^{[0]}$ difficult. PBP solution, instead, can handle efficiently complex geometries like the one of the abdomen by extracting all the *a priori* information collected in the transmit sensitivity magnitudes.

The global relative errors and the correlation coefficients of the recovered maps with respect to the expected results are reported in table 2. The dependence of the distributions estimation to the number of legs is less pronounced for the section of the abdomen than for the one of the head. Moreover, using the PBP solution as initial guess leads to results that are significantly better than those obtained after the same number

Table 2. Global relative errors and correlation coefficients of the maps of the abdomen section recovered on a 2 mm grid by CSI-GMT after 1000 iterative steps with input fields with 2 % of noise provided by 4, 8, and 16-legs TEM coils. Results obtained with both the initial conditions are reported.

	PBP solution				D'Urso's solution			
	ER[ε_r]	CC[ε_r]	ER[σ]	CC[σ]	ER[ε_r]	CC[ε_r]	ER[σ]	CC[σ]
4-legs	35 %	0.93	28 %	0.95	49 %	0.87	29 %	0.95
8-legs	31 %	0.94	26 %	0.96	81 %	0.74	38 %	0.92
16-legs	30 %	0.95	26 %	0.96	42 %	0.91	26 %	0.96

of iterations starting from D'Urso's solution.

6. Conclusion

A novel MREPT technique for measuring the EPs at RF by using MRI measurements has been proposed in this paper. Inspired by CSI-EPT [20], the proposed technique is a phaseless CSI-based [33] implementation of GMT [31], which uses only the measurable transmit sensitivity magnitude in the cost functional definition. This technique, referred to as CSI-GMT solves the issue of the non-measurable phase of the transmit sensitivity and prevents the introduction of *ad hoc* approximations for its estimation. Moreover, the PBP solution has been proposed as a new informative initial guess, in analogy to the classic back propagation solution. The particular realisation of the PBP solution described in this paper elaborates the measured magnitude of the transmit sensitivity, anyway the procedure that leads to this initial guess can be pursued also in the context of the traditional phaseless CSI technique, whose inputs are in general different from the one of CSI-GMT.

Numerical simulations on a realistic two-dimensional model problem show that, by using multiple linearly independent measurements as inputs, CSI-GMT converges towards the expected distributions without getting stuck on local minima of the cost functional. In addition, when multiple measurements are employed, the proposed method is robust against noisy inputs and coarse meshes, as it has already been proven elsewhere for CSI-EPT [35]. Furthermore, the proposed PBP solution turns out to be a very efficient initial guess compared to other strategies proposed in literature [45], which require the introduction of *a priori* knowledges often not available. In particular, the PBP solution automatically fits to domains with complex geometries, like in the case of the abdomen section. The good results obtained by elaborating multiple measurements of phaseless data suggest that CSI-GMT could be used effectively in parallel transmission MRI safety, thanks to the estimation of the auxiliary unknown $\vec{w}$ [34].

In this paper, CSI-GMT has been proposed without regularisation terms in the cost functional. Despite the method has proven to be robust against noise, the adoption of regularisation strategies could help handling the ill-posedness of the inverse problem as

well as introducing additional *a priori* information, which could reduce the probability to get stuck in a local minimum. The adoption of a regularisation strategy, like the classic additive or multiplicative total variation regularisation [32] or a geometrical segmentation-based one [10], should be further investigated. Another way to reduce the amount of local minima in the cost functional could be its reformulation taking into account the measurable relative phases between the transmit channels [28]. Finally, in order to validate *in vivo* the proposed technique, the operators should be implemented efficiently in three dimensions using proper software and hardware solutions.

References

[1] D. C. Sullivan, *et al.* 2015 Metrology standards for quantitative imaging biomarkers *Radiology* **277** 813–25

[2] S.-Y. Kim, J. Shin, D.-H. Kim, M. J. Kim, E.-K. Kim, H. J. Moon and J. H. Yoon 2016 Correlation between conductivity and prognostic factors in invasive breast cancer using magnetic resonance electric properties tomography (MREPT) *European Radiology* **26** 2317–26

[3] Z. Li 2016 A large-scale measurement of dielectric properties of normal and malignant colorectal tissues obtained from cancer surgeries at Larmor frequencies *Medical Physics* **43** 5991–7

[4] N. R. Datta, S. G. Ordóñez, U. S. Gaipl, M. M. Paulides, H. Crezee, J. Gellermann, D. Marder, E. Puric and S. Bodis 2015 Local hyperthermia combined with radiotherapy and/or chemotherapy: recent advances and promises for the future *Cancer Treatment Reviews* **41** 742–53

[5] R. W. Brown, Y.-C. N. Cheng, E. M. Haacke, M. R. Thompson and R. Venkatesan 2014 *Magnetic Resonance Imaging: Physical Principles and Sequence Design* (Hoboken, US-NJ: Wiley–Blackwell)

[6] H. P. Kok, P. Wust, P. R. Stauffer, F. Bardati, G. C. Van Rhoon and J. Crezee 2015 Current state of the art of regional hyperthermia treatment planning: a review *Radiation Oncology* **10** 196

[7] G. Tiberi, N. Fontana, M. Costagli, R. Stara, L. Biagi, M. R. Symms, A. Monorchio, A. Retico, M. Cosottini and M. Tosetti 2015 Investigation of maximum local specific absorption rate in 7 T magnetic resonance with respect to load size by use of electromagnetic simulations *Bioelectromagnetism* **36** 358–66

[8] D. Colton and R. Kress 2013 *Inverse Acoustic and Electromagnetic Scattering Theory* (*Applied Mathematical Sciences* vol 93) (New York, US-NY: Springer–Verlang)

[9] O. M. Bucci and T. Isernia 1997 Electromagnetic inverse scattering: retrievable information and measurement strategies *Radio Science* **32** 2123–37

[10] A. Rahimov, A. Litman and G. Ferrand 2017 MRI-based electric properties tomography with a quasi-Newton approach *Inverse Problems* **33** 105004

[11] A. Abubakar, G. Pan, M. Li, L. Zhang, T. M. Habashy and P. M. van den Berg 2011 Three-dimensional seismic full-waveform inversion using the finite-difference contrast source inversion method *Geophysical Prospecting* **59** 874–88

[12] M. Pastorino, A. Randazzo, A. Fedeli, A. Salvadé, S. Poretti, M. Maffongelli, R. Monleone and M. Lanini 2015 A microwave tomographic system for wood characterization in the forest products industry *Wood Material Science and Engineering* **10** 75–85

[13] A. Abubakar, W. Hu, P. M. van den Berg and T. M. Habashy 2008 A finite-difference contrast source inversion method *Inverse Problems* **24** 065004

[14] E. M. Haacke, L. S. Pepropoulos, E. W. Nilges and D. H. Wu 1991 Extraction of conductivity and permittivity using magnetic resonance imaging *Physics in Medicine & Biology* **36** 723–34

[15] U. Katscher, T. Voigt, C. Findeklee, P. Vernickel, K. Nehrke and O. Doessel 2009 Determination of electric conductivity and local SAR via B1 mapping *IEEE Transactions on Medical Imaging* **28** 1365–74

[16] T. Isernia, V. Pascazio and R. Pierri 2001 On the local minima in a tomographic imaging technique *IEEE Transactions on Geoscience and Remote Sensing* **39** 1596–607

[17] J. Liu, X. Zhang, S. Schmitter, P.F. Van de Moortele and B. He 2015 Gradient-based electric properties tomography (gEPT): a robust method for mapping electrical properties of biological tissues in vivo using magnetic resonance imaging *Magnetic Resonance in Medicine* **74** 634–46

[18] F. S. Hafalir, O. F. Oran, N. Gurler and Y. Z. Ides 2014 Convection-reaction equation based magnetic resonance electrical properties tomography (cr-MREPT) *IEEE Transactions on Medical Imaging* **33** 777–93

[19] H. Ammari, H. Kwon, Y. Lee, K. Kang and J. K. Seo 2015 Magnetic resonance-based reconstruction method of conductivity and permittivity distributions at the Larmor frequency *Inverse Problems* **31** 105001

[20] E. Balidemaj, C. A. T. Van den Berg, J. Trinks, A. L. H. M. W. Van Lier, A. J. Nederveen, L. J. A. Stalpers, H. Crezee and R. F. Remis 2015 CSI-EPT: a contrast source inversion approach for improved MRI-based electric properties tomography *IEEE Transactions on Medical Imaging* **34** 1788–96

[21] T. Nara, T. Furuichi and M. Fushimi 2017 An explicit reconstruction method for magnetic resonance electrical property tomography based on the generalized Cauchy formula *Inverse Problems* **33** 105005

[22] D. I. Hoult 2000 The principle of reciprocity in signal strength calculations—a mathematical guide *Concepts in Magnetic Resonance* **12** 173–87

[23] R. Stollberger and P. Wach 1996 Imaging of the active B1 field in vivo *Magnetic Resonance in Medicine* **35** 245–51

[24] L. I. Sacolick, F. Wiesinger, I. Hancu and M. W. Vogel 2010 B1 mapping by Bloch-Siegert shift *Magnetic Resonance in Medicine* **63** 1315–22

[25] A. L. H. M. W. Van Lier, D. O. Brunner, K. P. Pruessmann, D. W. J. Klomp, P. R. Luijten, J. J. W. Lagendijk and C. A. T. van den Berg 2012 B1+ phase mapping at 7 T and its application for in vivo electrical conductivity mapping *Magnetic Resonance in Medicine* **67** 552–61

[26] U. Katscher, C. Findeklee and T. Voigt 2012 B1-based specific energy absorption rate determination for nonquadrature radiofrequency excitation *Magnetic Resonance in Medicine* **68** 1911–8

[27] J. Liu, X. Zhang, P.-F. Van de Moortele, S. Schmitter and B. He 2013 Determining electrical properties based on B1 fields measured in an MR scanner using a multi-channel transmit/receive coil: a general approach *Physics in Medicine and Biology* **58** 4395–408

[28] X. Zhang, P.-F. Van de Moortele, S. Schmitter and B. He 2013 Complex B1 mapping and electrical properties imaging of the human brain using a 16-channel transceiver coil at 7 T *Magnetic Resonance in Medicine* **69** 1285–96

[29] D. K. Sodickson, *et al.* 2012 Local Maxwell tomography using transmit-receive coil arrays for contact-free mapping of tissue electric properties and determination of absolute RF phase *Proceedings of the 20th Annual Meeting ISMRM* (Melbourne, AU-VIC)

[30] D. K. Sodickson, L. Alon, C. M. Deniz, N. B. Eliezer, M. Cloos, L. A. Sodickson, C. M. Collins, G. C. Wiggins and D. S. Novikov 2013 Generalized local Maxwell tomography for mapping of electrical property gradients and tensors *Proceedings of the 21st Annual Meeting ISMRM* (Salt Lake City, US-UT)

[31] J. E. C. Serrallés, L. Daniel, J. K. White, D. K. Sodickson, R. Lattanzi and A. G. Polimeridis 2016 Global Maxwell tomography: a novel technique for electrical properties mapping based on MR measurements and volume integral equation formulations *Proceedings of the 2016 IEEE Antennas and Propagation Society International Symposium, APSURSI 2016* (Fajardo, PR) pp 1395–6

[32] P. M. Van den Berg and A. Abubakar 2001 Contrast source inversion method: state of art *Progress in Electromagnetic Research* **34** 189–218

[33] L. Li, H. Zheng and F. Li 2009 Two-dimensional contrast source inversion method with phaseless data: TM case *IEEE Transactions on Geoscience and Remote Sensing* **47** 1719–36

[34] A. Arduino, M. Chiampi, L. Zilberti and O. Bottauscio 2017 Alternative approaches to magnetic resonance-based electric properties tomography and local specific absorption rate estimation *IEEE Transactions on Magnetics* **53** 5100108

[35] A. Arduino, M. Chiampi, F. Pennecchi, L. Zilberti and O. Bottauscio 2017 Monte Carlo method of uncertainty propagation in magnetic resonance-based electric properties tomography *IEEE Transactions on Magnetics* **53** 5100304

[36] E. Balidemaj, C. A. T. Van den Berg, A. L. H. M. W. Van Lier, A. J. Nederveen, L. J. A. Stalpers, H. Crezee and R. F. Remis 2017 B1-based SAR reconstruction using contrast source inversion–electric properties tomography (CSI-EPT) *Medical & Biological Engineering & Computing* **55** 225–33

[37] International Electrotechnical Commission (IEC) 2010 *Medical electrical equipment - Part 2-33: Particular requirements for the basic safety and essential performance of magnetic resonance equipment for medical diagnosis* IEC 60601-2-33 ed 3.0

[38] G. Tiberi, M. Costagli, L. Biagi, A. D. Ciantis, N. Fontana, R. Stara, M. R. Symms, M. Cosottini, R. Guerrini and M. Tosetti 2016 SAR prediction in adults and children by combining measured B1+ maps and simulations at 7.0 tesla *Journal of Magnetic Resonance Imaging* **44** 1048–55.

[39] A. Zakaria, C. Gilmore and J. LoVetri 2010 Finite-element contrast source inversion method for microwave imaging *Inverse Problems* **26** 115010

[40] A. Arduino, L. Zilberti, M. Chiampi and O. Bottauscio 2017 CSI-EPT in presence of RF-shield for MR-coils *IEEE Transactions on Medical Imaging* **36** 1396–404

[41] C. M. Collins, B. Yang, Q. X. Yang and M. B. Smith 2002 Numerical calculations of the static magnetic field in three-dimensional multi-tissue models of the human head *Magnetic Resonance Imaging* **20** 413–24

[42] R. A. Elliott 1993 *Electromagnetics: History, Theory, and Applications* (New York, US-NY: IEEE Press)

[43] A. Bossavit 1998 *Computational Electromagnetism* (San Diego, US-CA: Academic Press)

[44] A. N. Kolmogorov and S. V. Fomin 1999 *Elements of the Theory of Functions and Functional Analysis* (Mineola, US-NY: Dover publications)

[45] M. D'Urso, K. Belkebir, L. Crocco, T. Isernia and A. Litman 2008 Phaseless imaging with experimental data: facts and challenges *Journal of the Optical Society of America A* **25** 271–81

[46] F. Seifert, G. Wübbeler, S. Junge, B. Ittermann and H. Rinneberg 2007 Patient safety concept for multichannel transmit coils *Journal of Magnetic Resonance Imaging* **26** 1315–21

[47] J. T. Vaughan and J. R. Griffiths 2012 *RF coils for MRI* (*Encyclopedia of Magnetic Resonance*) (Chichester, UK: John Wiley & Sons)

[48] M.-C. Gosselin, *et al.* 2014 Development of a new generation of high-resolution anatomical models for medical device evaluation: The Virtual Population 3.0 *Physics in Medicine and Biology* **59** 5287–303

[49] S. Gabriel, R. W. Lau and C. Gabriel 1996 The dielectric properties of biological tissues: III. Parametric models for the dielectric spectrum of tissues *Physics in Medicine and Biology* **41** 2271–93

[50] P. A. Hasgall, F. Di Gennaro, C. Baumgartner, E. Neufeld, M. C. Gosselin, D. Payne, A. Klingenbck, N. Kuster 2016 *ITIS Database for thermal and electromagnetic parameters of biological tissues Version 3.1.* [Online: `www.itis.ethz.ch/database`]

[51] M. Frigo and S. G. Johnson 2005 The design and implementation of FFTW3 *Proceedings of the IEEE* **93** 216–31